The measurement of ultrasound backscattering from cell pellet biophantoms and tumors *ex vivo*

Aiguo Han, Rami Abuhabsah, Rita J. Miller, Sandhya Sarwate, and William D. O'Brien, Jr.[a)]
Bioacoustics Research Laboratory, Department of Electrical and Computer Engineering, University of Illinois at Urbana-Champaign, 405 North Mathews, Urbana, Illinois 61801

(Received 7 January 2013; revised 23 April 2013; accepted 29 April 2013)

Simple scattering media fit scattering model theories much better than more complex scattering media. Tissue is much more complex as an acoustic scattering media and to date there has not been an adequate scattering model that fits it well. Previous studies evaluated the scattering characteristics of simple media (grouping of cells at various number densities) and fit them to the concentric spheres scattering model theory. This study is to increase the complexity of the media to provide insight into the acoustic scattering characteristics of tissue, and specifically two tumor types. Complementing the data from the tumors is 100% volume fraction cell pellets of the same cell lines. Cell pellets and *ex vivo* tumors are scanned using high-frequency single-element transducers (9–105 MHz), and the attenuation and backscatter coefficient (BSC) are estimated. BSC comparisons are made between cell pellets and tumors. The results show that the 4T1 (ATCC #CRL-2539) cell pellets and tumors have similar BSC characteristics, whereas the MAT (ATCC #CRL-1666) cell pellets and tumors have significantly different BSC characteristics. Factors that yield such differences are explored. Also, the fluid-filled sphere and the concentric spheres models are evaluated against the BSC characteristics, demonstrating that further work is required.
 [http://dx.doi.org/10.1121/1.4807576]

PACS number(s): 43.80.Cs, 43.80.Qf, 43.80.Vj [CCC] Pages: 686–693

I. INTRODUCTION

The purpose of this study is to understand the scattering process in tumors by comparing the ultrasound backscattering from tumors *ex vivo* to that from cell pellets of the same cell types. Understanding the scattering process is essential to quantitative ultrasound (QUS)—a quantitative imaging modality with a track record of success for uniquely identifying and classifying disease and monitoring treatments (Lizzi *et al.*, 1983; Miller *et al.*, 1983; Insana *et al.*, 1991; Insana *et al.*, 1993; Tamirisa *et al.*, 2001; Coleman *et al.*, 2004; Oelze and O'Brien, 2006; Oelze and Zachary, 2006; Vlad *et al.*, 2009; Mamou *et al.*, 2011). QUS utilizes the frequency-dependent information to yield quantitative estimates of tissue properties such as scatterer size, shape, number density, and acoustic impedance. To do so, a model-based approach is used, which requires the development of ultrasonic scattering models that match the anatomic geometry of the tissue type under investigation. However, understanding the acoustic scattering process in tissue/tumors and developing models that match the anatomic geometry is a challenging problem because of the complexity of biological structures. A reasonable and step-wise approach to understand the scattering process is to compare the strengths and weaknesses of simple models (individual cells), moderately complex models (groupings of cells at various concentrations), and significantly complex models (actual tissue/tumors).

Baddour *et al.* (2005) performed successful measurements of high-frequency (10–65 MHz) backscatter from single eukaryotic cells and proposed an anatomy-matching model where a cell is modeled as a single spherical scatterer with uniform mechanical properties that correspond to the cell nucleus. O'Brien *et al.* (2012) studied single-cell scattering further by imaging individual cells at higher frequencies (~200 MHz). In their study, individual cells were successfully resolved and estimates of attenuation and speed of sound for cell cytoplasm and nucleus were obtained.

For groupings of cells under various conditions, Tunis *et al.* (2005a) applied envelope statistics of ultrasound backscatter to determine the scatterer number density in dilute cell solutions. However, a statistical model was used that assumed point scatterers and the study did not deal with anatomic structure of groupings of cells. Teisseire *et al.* (2010) constructed cell pellet biophantoms that were composed of cells embedded in a plasma-thrombin supportive background and proposed an anatomy-matching model—the concentric spheres scattering model—wherein a eukaryotic cell was modeled as concentric fluid spheres, with the inner sphere and outer shell modeling the cell nucleus and cytoplasm, respectively. The backscatter coefficient (BSC) estimates from the biophantoms were shown to agree with the two concentric fluid spheres theory (McNew *et al.*, 2009) for relatively low cell concentrations (cell volume fraction <3%). In a further study (Han *et al.*, 2011), cell pellet biophantoms of higher cell concentrations (cell volume fraction ranging from 9.6% to 63%) were investigated. The concentric spheres model was found to become less applicable for estimating QUS parameters as the cell concentration increased, suggesting that the scattering model became less reliable as the complexity increased with cell concentration.

Previous studies progressed from simple (individual cells) to moderate complexity (groupings of cells). This study aims to transit from moderate to significant complexity

[a)]Author to whom correspondence should be addressed. Electronic mail: wdo@uiuc.edu

(real tumors) and make a comparison between the degrees of complexity. Although the ultimate goal is to model the ultrasound scattering in tissue and tumors *in vivo*, this paper focuses on the comparisons between biophantoms and tumors with the view that such comparisons will provide insights into tumor scattering. To mimic tumors, the concentration of the biophantoms was chosen to be the highest; the biophantoms are made of densely packed cells without supportive materials. The dense cell pellet has actually been used as a model of real tissues/tumors for high-frequency QUS studies due to its simplicity of preparation and ease of implementation (Tunis *et al.*, 2005b; Oelze and Zachary, 2006). However, the cell pellet and tumors are different in many ways, which could make their ultrasound backscatter differ from each other. The tumors have more complex components and structures than cell pellets. There are cells, complex extracellular matrix, and vasculatures in a tumor, whereas there are only cells in a cell pellet. The scattering from the tumor will be even more complex if there are regions of necrosis or apoptosis. In the present study, the BSC and attenuation are estimated for cell pellets and tumors *ex vivo* from two cell lines using high-frequency single-element transducers (9–105 MHz). For each cell line, comparisons between the cell pellets and tumors are performed. Two existing models, the fluid-filled sphere model (Anderson, 1950) and the concentric spheres model (McNew *et al.*, 2009), are evaluated on the BSC data from both cell pellets and tumors.

II. MATERIALS AND METHODS

A. Biophantom construction

The cell pellet biophantoms were composed of a large number (cell volume fraction close to 100%) of densely packed cells without any supportive background materials. Two tumor cell lines, the 13762 MAT B III (MAT) mammary adenocarcinoma [American Type Culture Collection (ATCC) #CRL-1666, Manassas, VA] and the 4T1 mammary carcinoma (ATCC #CRL-2539), were used to create the cell pellets, each cell line having five independent replicates of cell pellets. The two cell lines were chosen because they are commonly used rapid-growing rodent models of human breast cancer. Also, their scant extracellular matrix makes them ideal for the purpose of this study.

The two cell lines were both cultured in an ATCC-recommended medium along with 8.98% of fetal bovine or calf serum (ATCC) and 1.26% of antibiotic (Hyclone Laboratories, Logan, UT). The cells were grown in three 225-cm^2 cell culture flasks (BD Biosciences, Bedford, MA). When the flasks reached 80%–90% confluency, a large number of cells were collected as a cell suspension. A Reichert Bright-Line® hemacytometer (Hausser Scientific, Buffalo, NY) was used to count viable cells to yield the number of cells per known volume. Equal volumes of the dye Trypan Blue (HyClone Laboratories, Logan, UT) and cell suspension were gently mixed by pipetting and then added into the counting chambers of the hemacytometer. Trypan Blue was used to differentiate nonviable cells (stained as blue cells) from viable cells (displayed as bright cells). At this point, each cell pellet had an average of over 95% live cell viability. A known number of viable cells was placed in a 50-mL conical centrifuge tube (Corning® Incorporated, Corning, NY) and spun in a 4 °C centrifuge at 2500 rpm for 10 min, and the supernatant was removed. The 50-mL conical tube was centrifuged again at 4 °C and 2500 rpm for 3 min, and the supernatant was removed. A heated surgical blade was used to cut off the top portion of the 50-mL centrifuge tube 1 cm above the remaining cell sediment. A spatula was used to collect the cell sediment and place it on a planar Plexiglas® plate. After a 10-min wait, the cell sediment and Plexiglas® plate were carefully submerged in Dulbecco's Phosphate Buffered Saline (DPBS) (Sigma-Aldrich®, MO) for ultrasonic scanning.

B. Animal use, cell injection, and tumor sample preparation

Twelve Fischer 344 rats and 12 BALB/c mice were purchased from Harlan® Laboratories, Inc. (Indianapolis, IN). The MAT and 4T1 cells were injected into the rats and mice, respectively. The animals were anesthetized with isoflurane prior to cell injection. A volume of 100 μL containing 500 cells was injected subcutaneously, bilaterally in the mammary fat pad. The size of tumors was regularly monitored *in vivo* both manually and using a VisualSonics Vevo® 2100 system (VisualSonics Inc., Toronto, ON, Canada). Tumors were allowed to grow until they had reached about 5 mm in diameter. The animals were then euthanized via CO_2 and the tumors were excised and placed on a planar Plexiglas® plate. The tumors and the Plexiglas® plate were submerged in DPBS for ultrasonic scanning. If the thickness of the excised tumor exceeded 2 mm, the top and bottom surfaces of the tumor were cut flat such that the thickness of the tumor did not exceed 2 mm. This was done to reduce total attenuation and achieve a good signal-to-noise ratio for the insertion-loss attenuation measures. Eventually 13 MAT tumors and 15 4T1 tumors were successfully excised, scanned, and analyzed.

The experimental protocol was approved by the Institutional Animal Care and Use Committee of the University of Illinois and satisfied all campus and National Institutes of Health rules for the humane use of laboratory animals. Animals were housed in an Association for Assessment and Accreditation of Laboratory Animal Care (Rockville, MD), an approved animal facility, and provided food and water *ad libitum*.

C. Ultrasound scanning procedure and BSC estimation method

Three single-element, weakly focused transducers (20-MHz transducer IS2002HR, from Valpey Fisher Cooperation, Hopkinton, MA; 40 - and 80-MHz transducers from NIH High-frequency Transducer Resource Center, University of Southern California, Los Angeles, CA; see Table I) were used to scan the biophantoms and tumors. The entire frequency range was 9–105 MHz.

The transducers were interfaced with a UTEX UT340 pulser/receiver (UTEX Scientific Instruments Inc.,

TABLE I. Transducer information and characteristics.

Center frequency (MHz)	−10 dB bandwidth (MHz)	Wavelength at center frequency (μm)	f-number	−6 dB depth of field (mm)	−6 dB beam width (μm)	Acquisition step size (μm)
20	9–33	75.0	3.0	4.0	230	110
40	26–65	37.5	3.0	2.4	113	60
80	49–105	18.8	3.0	1.2	56.4	30

Mississauga, ON, Canada) that operated in the pitch-catch mode. A 50DR-001 BNC attenuator (JFW Industries Inc., Indianapolis, IN) was connected to the pulser to attenuate the driving pulse in order to avoid transducer saturation. A RDX-6 diplexer (Ritec Inc., Warwick, RI) was used to separate the transmitted and received signals because only the transmitted signal needed to be attenuated. The received radiofrequency (RF) signals were acquired using a 10-bit Agilent U1065A-002 A/D card (Agilent Technologies, Santa Clara, CA) set to sample at 1 GHz. The transducers were moved using a precision motion control system (Daedal Parker Hannifin Corporation, Irwin, PA) that has a linear spatial accuracy of 1 μm. The samples were placed on the Plexiglas® plate during ultrasound scans. The scans were performed in a small tank filled with DPBS at room temperature (Fig. 1).

Attenuation and BSC measurements were both performed for each sample. The attenuation was measured using an insertion-loss broadband technique (Wear *et al.*, 2005). The transducer focus was positioned at the sample-Plexiglas® interface. The insertion loss was determined by comparing the power spectrum of the echo reflected off the Plexiglas surface with and without the sample being inserted in the ultrasound path. The effect of DPBS attenuation was compensated for. The attenuation (dB/cm) of the sample was generated by averaging the attenuation obtained from 36 independent locations across the sample.

The BSC scanning procedure started with acquiring a reference scan from the planar Plexiglas® plate whose pressure reflection coefficient relative to DPBS at room temperature is known (=0.37). The reference scan was taken by recording the reflection off the DPBS-Plexiglas® interface at the set of positions that covered the −6 dB depth of focus with a step size of a half wavelength. Next, a raster scan on the sample was performed with a lateral step size of a half beam width. The transducer focus was positioned in the sample. The scan covered a sufficient length in both the axial and lateral directions so that numerous regions of interest (ROIs) could be acquired and processed from each scan, where 11 independent scans were recorded for each sample. The number of A-lines for each scan varied depending on the transducer frequency and the size of the sample. The BSC was estimated using the method described in Chen *et al.* (1997). This method was designed to remove equipment-dependent effects. To generate a BSC vs frequency curve for a sample scanned by a single transducer, (i) a BSC estimate was made for each ROI based on the gated RF echo data from that ROI, (ii) a mean BSC was estimated for each of the 11 scans by averaging the BSCs from all the ROIs within that scan, and then (iii) the 11 mean BSCs were averaged. A power-law fit correction was made for the attenuation within each sample.

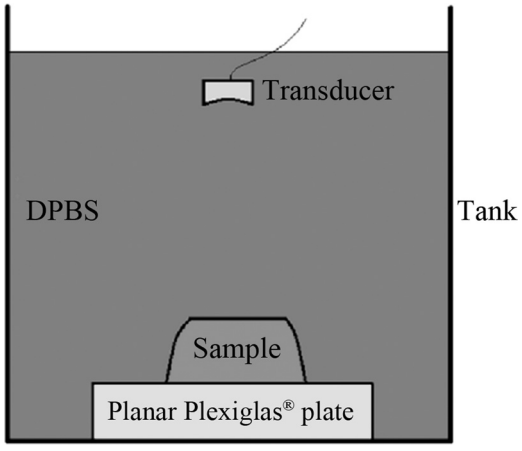

FIG. 1. The diagram of the experimental setup.

D. Histology processing

Immediately after scanning, the sample was placed into a histology processing cassette and fixed by immersion in 10% neutral-buffered formalin (pH 7.2) for a minimum of 12 h for histopathologic processing. The sample was then embedded in paraffin, sectioned, mounted on glass slides, and stained with hematoxylin and eosin for histopathologic evaluation (by the pathologist, S.S.) by light microscopy (Olympus BX–51, Optical Analysis Corporation, Nashua, NH).

E. Scattering models

Two scattering models were evaluated against the BSC results: the fluid-filled sphere model and the concentric spheres model (Teisseire *et al.*, 2010; Fig. 2). For a collection of n randomly positioned scatterers with *identical* size insonified by a plane wave of amplitude P_0, the theoretical BSC can be expressed as

$$\mathrm{BSC}(f) = \frac{n}{V}\frac{r^2|p_{\mathrm{scat,i}}(\theta=\pi)|^2}{P_0^2}, \quad (1)$$

where r is the distance from the scatterers to the observation point, which is assumed to be very large compared to the dimensions of the scattering volume, V is the scattering volume, the factor n/V (also denoted as $\bar{n}$) corresponds to the scatterer number density of the ensemble, and $|p_{\mathrm{scat,i}}(\theta=\pi)|$

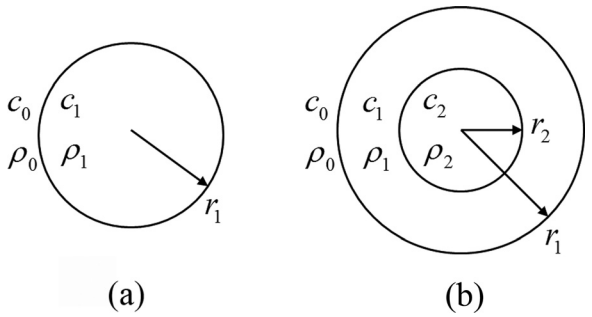

FIG. 2. Geometry of a single scatterer for the fluid-filled sphere model (a), and concentric spheres model (b). For both (a) and (b), the infinite (background) medium has density ρ_o and sound speed c_o. In (a), the sphere has density ρ_1, sound speed c_1, and radius r_1. In (b), the outer sphere has density ρ_1, sound speed c_1, and radius r_1. The inner sphere has density ρ_2, sound speed c_2, and radius r_2. The respective impedances are $Z_o = \rho_o c_o$, $Z_1 = \rho_1 c_1$, and $Z_2 = \rho_2 c_2$. The three media (inner sphere, outer sphere, and background) are each modeled as spatially homogeneous fluids.

is the amplitude of the backscattered wave from an individual scatterer. The term $|p_{\text{scat,i}}(\theta = \pi)|$ can be calculated using Eq. (10) of Anderson (1950) and Eq. (3) of McNew *et al.* (2009) for single fluid sphere scatterer and two concentric fluid spheres scatterer, respectively.

The distribution of scatterer sizes must be considered in practice. For this study, the scatterer radius for the fluid-filled sphere model is assumed to follow the Gaussian distribution (consider only the range of $[\mu - 3\sigma, \mu + 3\sigma]$ for numerical implementation). For the concentric sphere model, however, the radii of the inner and outer spheres are assumed to follow Gaussian distributions, and a linear correlation ($r_1 = C_1 r_2 + C_2$) between the inner and outer radii is also assumed. Under these assumptions, the BSC can be calculated by

$$\text{BSC}_{\text{dist}}(f) = \int_0^\infty g(r) \cdot \text{BSC}(f, r)\, dr, \tag{2}$$

where $g(r)$ is the probability density function of the sphere radius (sphere radius r_1 for the fluid-filled sphere model, or inner sphere radius r_2 for the concentric spheres model).

F. *B*-spline fit

In order to model the shape trend of the experimental BSC curves, *B*-splines are fit to the log BSC vs frequency curves over the entire frequency range (9–105 MHz). *B*-spline is a commonly used smoothing spline for large data sets. The advantage of a smoothing spline is that the resulting curve is not required to pass through each data point. The resulting *B*-spline curve is a linear combination of *M* *B*-spline basis functions, where *M* is the degrees of freedom, and the *B*-spline basis functions are spaced at different locations to provide local shape control. In this study, we fit cubic *B*-splines with five degrees of freedom, giving us five *B*-spline basis curves at five equally spaced locations in the frequency range. The best-fit *B*-spline is then a linear combination of five *B*-spline basis functions

$$bs(f) = \sum_{i=1}^{5} \beta_i b_i(f), \tag{3}$$

where $b_i(f)$ is the ith *B*-spline basis function, and β_i is the corresponding coefficient of each basis function to control the shape locally. The calculation of $b_i(f)$ and the least square estimation of β_i are performed in the *R* statistical package.

III. RESULTS

A. BSC results

The attenuation-compensated BSC estimates from both cell pellets and tumors are shown in Fig. 3 for each cell type. The BSC curves are presented in a fashion that the curve from each individual realization of each sample type is shown. This type of presentation allows one to infer how large the measurement uncertainty is. For instance, the five MAT cell pellet curves in Fig. 3(b) appear to have the narrowest distribution. This can serve as an indication of the upper limit of measurement uncertainty. One may also note that the MAT tumors have a much wider distribution in BSC curves. Such a wide distribution in MAT tumors can then be reasonably attributed to large inter-tumor variation rather than measurement uncertainty if we consider the upper limit of measurement uncertainty indicated by the MAT cell pellet data. Overall, it is observed that tumors have a wider BSC distribution than that of cell pellets for both cell lines because the cell pellets are well-controlled biophantoms, whereas tumors are less controlled and thus have larger

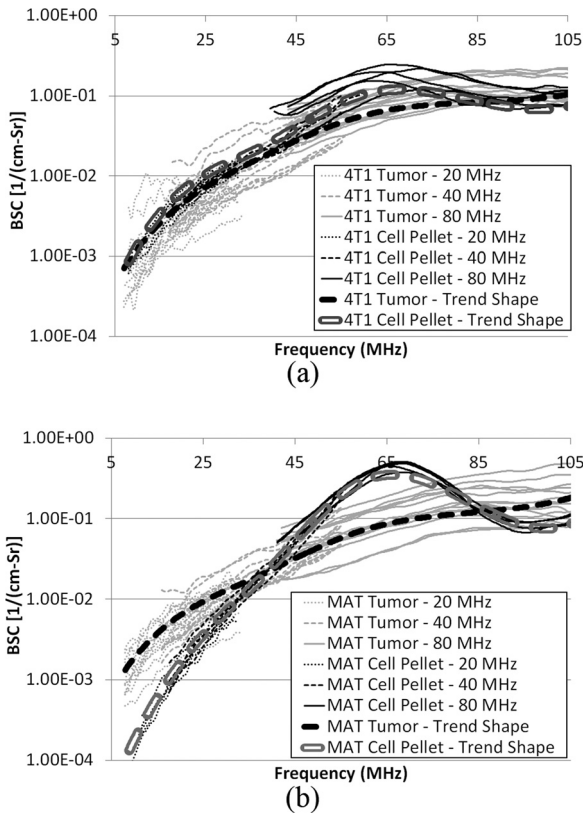

FIG. 3. BSC vs frequency for (a) five 4T1 cell pellets (in thinner black) and fifteen 4T1 tumors (in thinner gray), and (b) five MAT cell pellets (in thinner black) and thirteen MAT tumors (in thinner gray). The *B*-spline curves (tumors in thicker dashed black; cell pellets in gray rectangles) show the trend shapes.

variance in nature. Also shown in Fig. 3 are the four BSC shape trends represented by the *B*-spline curves.

To compare tumors against cell pellets, the two charts of Fig. 3 are examined separately. Figure 3(a) shows that, for the 4T1 cell line, the tumors and cell pellets share similar BSC values over the entire frequency range under investigation except around 65 MHz, where the BSC of the cell pellets is slightly higher than that of the tumors. There appears to be a slight but noticeable peak at 65 MHz for the cell pellet BSC, whereas the BSC curves are flatter for tumors. Overall, the BSC shapes and magnitude are similar for 4T1 cell pellets and tumors. However, this is not true for the MAT cell line. Figure 3(b) shows two distinct BSC shape trends. Before attempting to explain such distinction between MAT cell pellets and MAT tumors, the attenuation results and histopathologic evaluation of cell pellets and tumors are presented in Secs. III B and III C, respectively.

B. Attenuation

The attenuation (dB/cm) results are presented in Fig. 4 as a function of frequency. In Fig. 4(a), the 4T1 cell pellet attenuation curves are not readily separable from those of the 4T1 tumors. However, the MAT cell pellet attenuation curves are completely separated from the MAT tumor attenuation curves [Fig. 4(b)].

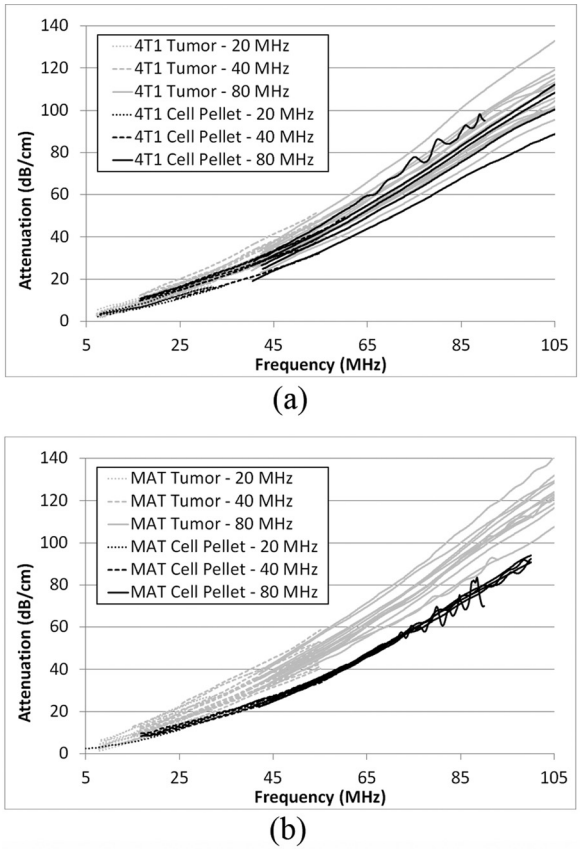

FIG. 4. Attenuation vs frequency for (a) five 4T1 cell pellets (in black) and fifteen 4T1 tumors (in gray), and (b) five MAT cell pellets (in black) and thirteen MAT tumors (in gray).

C. Histology

No apparent difference is observed between the histological images of the 4T1 cell pellets and 4T1 tumors. The microscopic features of the 4T1 cells in these two types of preparations are similar. Extracellular matrix is scant and minimal necrosis is seen.

However, for the MAT cell line, interesting observations are made. First, various degrees of necrosis are observed in the MAT tumors, and the necrotic regions are dispersed over the tumor. Second, there are a few blood vessels with intra luminal red blood cells, and lymphocytes.

D. Model fitting

Because one of our goals is to find an anatomy-matching scattering model for tumors, two existing models, the fluid-filled sphere model and the concentric spheres model, were evaluated relative to the BSC data. A best-fit BSC was determined with each model for each of the four BSC groups (4T1 cell pellet, 4T1 tumor, MAT cell pellet, and MAT tumor; Figs. 5 and 6). The fitting was performed using the least-squares technique, where the MATLAB (The Mathworks Inc., Natick, MA) nonlinear curve-fitting function "lsqcurvefit" was used specifically. Gaussian size distribution was assumed for both models (Han *et al.*, 2011). The results show that neither model is capable of precisely catching the trends of BSC curves except for the case of Fig. 6(c).

IV. DISCUSSION

The 4T1 cell pellets and tumors have been shown to be similar: they have similar histopathologic features and similar ultrasonic characteristics (specifically BSC and attenuation). The similar ultrasonic characteristics are likely caused by the similar histopathologic features. In terms of histopathologic features, the 4T1 cells have similar sizes and shapes in the cell pellet form and in tumors. Also, the 4T1 cell pellets and tumors have similar components: the cell pellets are composed of tumor cells only, and the tumors are mainly composed of tumor cells with little extracellular matrix. In terms of ultrasonic characteristics, it is observed that the 4T1 cell pellets and tumors have similar BSC and attenuation estimates. The observed similarity in BSC could be interpreted by the hypothesis that the 4T1 cell pellets and tumors have similar scattering sites (whether being cell nuclei or whole cells, or a combination of both) given their similar components. The observed similarity in attenuation could be analyzed in two aspects: the scattering and the absorption (note: attenuation is the combined effect of both scattering and absorption). The scattering from 4T1 cell pellets and tumors has been shown to be similar in terms of BSC. The absorptions are speculated to be similar based on the observation that 4T1 cell pellets and tumors have similar components and that acoustic absorption occurs primarily at the macromolecular level. With similar BSCs and absorptions, it makes sense that the attenuation estimates are found to be similar for 4T1 cell pellets and tumors. Therefore, the similarity in ultrasonic characteristics is a result of the similarity in histopathologic features. 4T1 is an example where the

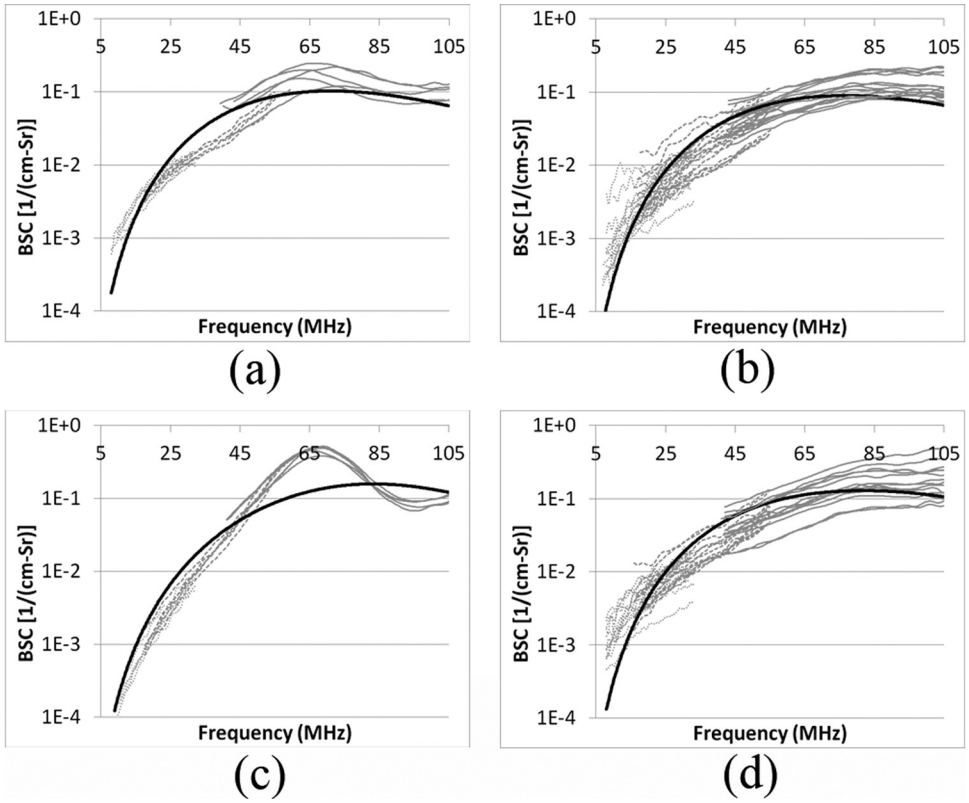

FIG. 5. The best-fit fluid-fill sphere BSC (in black) for (a) 4T1 cell pellets, (b) 4T1 tumors, (c) MAT cell pellets, and (d) MAT tumors. The experimental BSC curves are in gray.

tumor has relatively simple scattering structures such that the scattering from the tumor is similar to that from the cell pellet.

In contrast to 4T1, the MAT cell pellets and tumors show different BSC and attenuation estimates, which can be attributed to their different histopathologic features. The main difference between MAT cell pellets and tumors histologically is that regions of necrosis were found in MAT tumors, but not in MAT cell pellets. The scatterers are significantly different in necrotic regions than other regions where tumor cells are intact. There are no scatterers that are as big as tumor cells or cell nuclei in necrotic regions. The necrotic

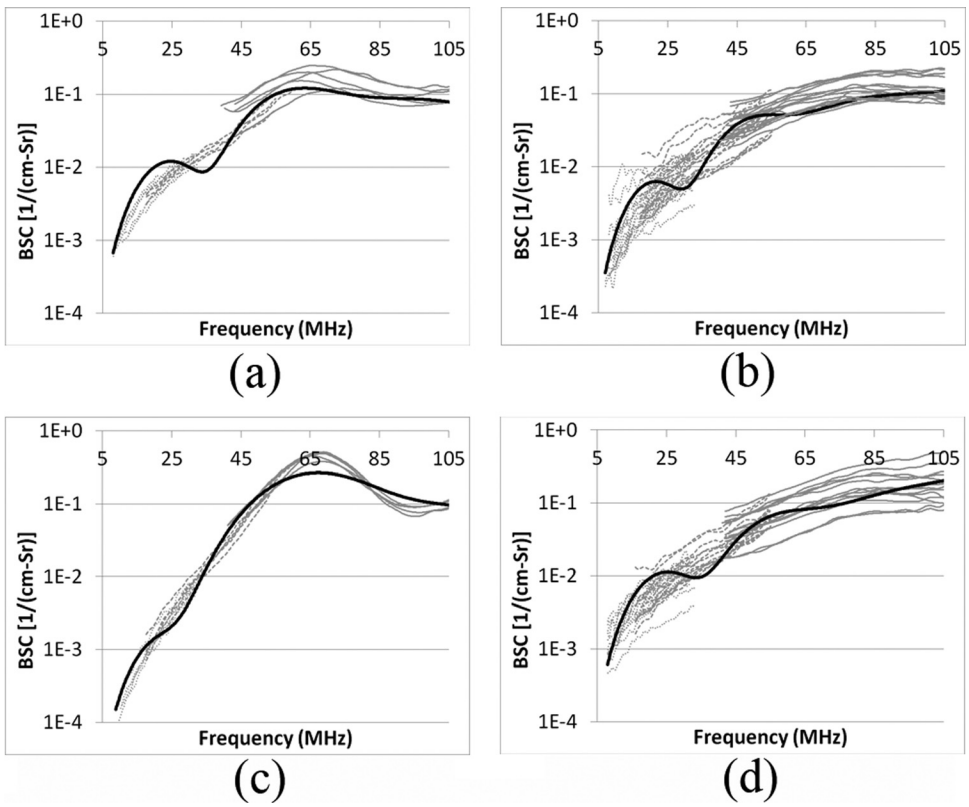

FIG. 6. The best-fit concentric spheres BSC (in black) for (a) 4T1 cell pellets, (b) 4T1 tumors, (c) MAT cell pellets, and (d) MAT tumors. The experimental BSC curves are in gray.

areas consist of fragmented cytoplasm and nuclei rather than intact nuclei and cytoplasm with definite shape. This fragmented cellular material is of variable size. Therefore, necrosis can be an important factor causing the BSC estimates to be significantly different in the MAT tumors vs cell pellets. In addition to BSC, the absorptions are likely to be different as well, due to necrosis in MAT tumors. With different BSCs and absorptions, it makes sense that the attenuation estimates are different for MAT cell pellets and tumors. Therefore, MAT is an example where the tumor is more complex than the cell pellet and the anatomic structures such as necrosis are playing a role in scattering.

The MAT and 4T1 results demonstrate that cell pellets and solid tumors grown from the same cells injected subcutaneously in animals do not necessarily have similar ultrasonic characteristics. The ultrasonic characteristics are similar only when the tumor contains primarily tumor cells. This finding is more comprehensive than previous findings (Oelze and Zachary, 2006; Taggart *et al.*, 2007) which suggested that cell pellets and tumors have very similar ultrasonic characteristics. First, those studies did not directly compare the BSC of the cell pellets and tumors. Rather, a specific model-based QUS parameter was studied and shown to be similar for the cell pellets and tumors. The similarity in QUS parameters does not necessarily imply the similarity in BSC. Second, the cell lines used in Oelze and Zachary (2006) happened to be 4T1 such that the tumors had little necrosis or additional components besides tumor cells. Tumors that have more complex scattering structures were not included in those studies.

The comparison between tumors and cell pellets of the same cell lines has provided insights into the scattering in tumors: (1) the 4T1 result is encouraging in the sense that it demonstrates the scattering from tumors of homogeneous morphology can be as similar as the scattering from the cell pellets of the same cell lines. The scattering model theories for such tumors can be developed directly by studying the cell pellets; (2) the MAT result improves our understanding of tumor scattering in the sense that it demonstrates the important role of tumor anatomic details on scattering for tumors with heterogeneous morphology and complex scattering structures.

In addition to the cell pellet vs tumor comparison, the comparison between cell pellets of different cell lines also provides valuable information. The 4T1 and MAT cell pellets are observed to have distinct BSC curves (Fig. 3). This observation is made because the two different cell types have different sizes and acoustic properties. This observation is encouraging as it is the basis to QUS: in order for QUS to be working, there must be a difference in a fundamental ultrasonic parameter, such as the BSC, for different cell types, and such a difference must be experimentally measurable.

From a modeling point of view, two factors must be taken into account for tumors as suggested by the above discussion. The cell type is a primary factor; 4T1 and MAT cell pellets have distinct BSC curves. The anatomic detail of the tumor is another factor; it is not sufficient to only consider the tumor cells as the scattering source if the anatomic structure is more complex, such as what is seen in the MAT tumors.

The evaluation of two existing models (the fluid-filled sphere and the concentric spheres) on both cell pellet and tumor BSCs suggests that further work on modeling is needed. The observation that neither model fits well the cell pellet data can be attributed to the fact that the models only sum up the scattering power from individual scatterers without considering the acoustic interactions between scatterers (multiple scattering and coherent scattering). If there were a significant source of coherent scattering, the shape of BSC curves would be different; the BSC magnitude would become higher at frequencies of constructive interference and become lower at frequencies of destructive interference, compared to the BSC magnitude without coherent scattering. An example of how coherent scattering in cell pellets might change the BSC curves can be found from a previous publication (Han *et al.*, 2011). Future work is directed to developing models that take into account the cell type, interaction among scatterers, and anatomic detail in the tumor.

V. CONCLUSIONS

The comparison in BSC between tumors and cell pellets of the same cell lines improves our fundamental understanding of tumor scattering; the scattering from tumors is affected by both cell types and tumor anatomic details. Such a comparison also provides a tool of identifying unique tumor scattering structures. Neither of the two theoretical models evaluated in this study is adequate for modeling the tumor or cell pellet scattering. Further work in modeling tumor scattering is required and directed toward combining both cell types and tumor anatomic details.

ACKNOWLEDGMENTS

This work was supported by NIH Grant No. R01CA111289. The authors would like to thank Ellora Sen-Gupta for her assistance with cell culture and Matt Lee for his assistance with cell injection and tumor excision.

Anderson, V. C. (**1950**). "Sound scattering from a fluid sphere," J. Acoust. Soc. Am. **22**, 426–431.

Baddour, R. E., Sherar, M. D., Hunt, J. W., Czarnota, G. J., and Kolios, M. C. (**2005**). "High-frequency ultrasound scattering from microspheres and single cells," J. Acoust. Soc. Am. **117**, 934–943.

Chen, X., Phillips, D., Schwarz, K. Q., Mottley, J. G., and Parker, K. J. (**1997**). "The measurement of backscatter coefficient from a broadband pulse-echo system: A new formulation," IEEE Trans. Ultrason. Ferroelectr. Freq. Control. **44**, 515–525.

Coleman, D. J., Silverman, R. H., Rondeau, M. J., Boldt, H. C., Lloyd, H. O., Lizzi, F. L., Weingeist, T. A., Chen, X., Vangveeravong, S., and Folberg, R. (**2004**). "Noninvasive *in vivo* detection of prognostic indicators for high-risk uveal melanoma: Ultrasound parameter imaging," Ophthalmology **111**(3), 558–564.

Han, A., Abuhabsah, R., Blue, J. P., Jr., Sarwate, S., and O'Brien, W. D., Jr. (**2011**). "Ultrasonic backscatter coefficient quantitative estimates from high-concentration Chinese hamster ovary cell pellet biophantoms," J. Acoust. Soc. Am. **130**, 4139–4147.

Insana, M. F., Hall, T. J., and Fishback, J. L. (**1991**). "Identifying acoustic scattering sources in normal renal parenchyma from the anisotropy in acoustic properties," Ultrasound Med. Biol. **17**, 613–626.

Insana, M. F., Hall, T. J., Wood, J. G., and Yan, Z. Y. (**1993**). "Renal ultrasound using parametric imaging techniques to detect changes in microstructure and function," Invest. Radiol. **28**(8), 720–725.

Lizzi, F. L., Greenebaum, M., Feleppa, E. J., Elbaum, M., and Coleman, D. J. (**1983**). "Theoretical framework for spectrum analysis in ultrasonic tissue characterization," J. Acoust. Soc. Am. **73**(4), 1366–1373.

Mamou, J., Coron, A., Oelze, M. L., Saegusa-Beecroft, E., Hata, M., Lee, P., Machi, J., Yanagihara, E., Laugier, P., and Feleppa, E. J. (**2011**). "Three-dimensional high-frequency backscatter and envelope quantification of cancerous human lymph nodes," Ultrasound Med. Biol. **37**, 345–357.

McNew, J., Lavarello, R., and O'Brien, W. D., Jr. (**2009**). "Sound scattering from two concentric fluid spheres," J. Acoust. Soc. Am. **122**, 2968.

Miller, J. G., Perez, J. E., Mottley, J. G., Madaras, E. I., Johnston, P. H., Blodgett, E. D., Thomas, L. J., III, and Sobel, B. E. (**1983**). "Myocardial tissue characterization: An approach based on quantitative backscatter and attenuation," Ultrasonics Symp. Proc. **2**, 782–793.

Oelze, M. L., and O'Brien, W. D., Jr. (**2006**). "Application of three scattering models to the characterization of solid tumors in mice," Ultrason. Imaging **28**, 83–96.

Oelze, M. L., and Zachary, J. F. (**2006**). "Examination of cancer in mouse models using high-frequency quantitative ultrasound," Ultrasound Med. Biol. **32**, 1639–1648.

O'Brien, W. D., Jr., Auger, T., Han, A., and Wirtzfeld, L. (**2012**). "Quantitative ultrasound microscopy imaging of cells," J. Acoust. Soc. Am. **131**, 3496.

Taggart, L. R., Baddour, R. E., Giles, A., Czarnota, G. J., and Kolios, M. C. (**2007**). "Ultrasonic characterization of whole cells and isolated nuclei," Ultrasound Med. Biol. **33**, 389–401.

Tamirisa, P. K., Holland, M. R., Miller, J. G., and Perez, J. E. (**2001**). "Ultrasonic tissue characterization: Review of an approach to assess hypertrophic myocardium," Echocardiogr. **18**(7), 593–597.

Teisseire, M., Han, A., Abuhabsah, R., Blue, J. P., Jr., Sarwate, S., and O'Brien, W. D., Jr. (**2010**). "Ultrasonic backscatter coefficient quantitative estimates from Chinese hamster ovary cell pellet biophantoms," J. Acoust. Soc. Am. **128**, 3175–3180.

Tunis, A. S., Baddour, R. E., Czarnota, G. J., Giles, A., Worthington, A. E., Sherar, M. D., and Kolios, M. C. (**2005a**). "Using high frequency ultrasound envelope statistics to determine scatterer number density in dilute cell solutions," Proc.-IEEE Ultrason. Symp. **2**, 878–881.

Tunis, A. S., Czarnota, G. J., Giles, A., Sherar, M. D., Hunt, J. W., and Kolios, M. C. (**2005b**). "Monitoring structural changes in cells with high frequency ultrasound signal statistics," Ultrasound Med. Biol. **31**(8), 1041–1049.

Vlad, R. M., Brand, S., Giles, A., Kolios, M. C., and Czarnota, G. J. (**2009**). "Quantitative ultrasound characterization of responses to radiotherapy in cancer mouse models," Clin. Cancer Res. **15**(6), 2067–2075.

Wear, K. A., Stiles, T. A., Frank, G. R., Madsen, E. L., Cheng, F., Feleppa, E. J., Hall, C. S., Kim, B. S., Lee, P., O'Brien, W. D., Jr., Oelze, M. L., Raju, B. I., Shung, K. K., Wilson, T. A., and Yuan, J. R. (**2005**). "Interlaboratory comparison of ultrasonic backscatter coefficient measurements from 2 to 9 MHz," J. Ultrasound Med. **24**, 1235–1250.